IOP Publishing | International Atomic Energy Agency Nuclear Fusion

Nucl. Fusion **61** (2021) 056006 (9pp) https://doi.org/10.1088/1741-4326/abebcd

Gyrokinetic simulation of turbulent transport for I-mode edge plasmas

Hongwei Yang[1], Tianchun Zhou[2,*] and Yong Xiao[1,*]

[1] Institute for Fusion Theory and Simulation, Zhejiang University, Hangzhou 310027, China
[2] School of Physics & Laboratory for Space Environment and Physical Science, Harbin Institute of Technology, Harbin 150001, China

E-mail: yxiao@zju.edu.cn and tczhou@hit.edu.cn

Received 17 December 2020, revised 12 February 2021
Accepted for publication 3 March 2021
Published 13 April 2021

Abstract

I-mode is an attractive candidate among the confinement regimes proposed for burning operation with good energy confinement similar to H-mode but poor particle confinement similar to L-mode, resulting in no obvious impurity accumulation and free of large edge localized modes. Although I-mode has been recently achieved experimentally on several tokamaks, theory and simulation remain insufficient to explain the mechanisms behind the I-mode formation and its peculiar transport behaviour. In this work, an electrostatic gyrokinetic simulation using gyrokinetic toroidal code (GTC) is carried out for the typical I-mode plasma profiles. Linear simulations reveal that two competitive instabilities coexist within the range of short and long wavelengths during I-mode phase, respectively. It is found that the passing electron response cannot be treated adiabatically for those modes with mode numbers close to that of weekly coherent mode, which is considered to be a major player in the I-mode formation and responsible for the unusual transport behaviour exhibited in I-mode plasmas. Nonlinear simulations yield a turbulent heat transport level that is comparable to the experimental level, and about a half of the experimental particle transport level.

Keywords: I-mode, WCM, zonal flow, geodesic acoustic mode, L–I transition, turbulent transport

(Some figures may appear in colour only in the online journal)

1. Introduction and simulation model

I-mode is an intermediate confinement regime in tokamaks between L-mode and H-mode, which was first discovered on ASDEX Upgrade [1] as a transient regime and originally named 'improved L-mode'. During the last decade, researchers on the Alcator C-Mod tokamak have developed I-mode into a stationary operation regime with its lifetime more than 10 times of the energy confinement time τ_E [2]. What makes this regime most special and intriguing is that the energy and particle transport channels in the edge region are decoupled, i.e., it exhibits low energy transport across the last closed flux surface, while higher particle transport than that of energy. Furthermore, this regime is free of explosive edge localized modes (ELMs) and as a result of high level of particle transport, there is no apparent impurity accumulation. Thus I-mode is often considered to be an alternative regime for burning plasma operation in parallel with the conventional ELMy or ELM-free H-mode, which needs extra control of impurity accumulation level and strategies for heavy impurities and helium ash removal to avoid significant energy confinement deterioration. To create an I-mode experimentally, plasma discharge starts with L-mode in the magnetic geometry with unfavourable ion $B \times \nabla B$ drift, then L–I transition takes place when plasmas are heated with power threshold two times higher than that needed for the direct L–H transition in favourable magnetic geometry [2–5]. During this process the edge plasma temperature gradient especially for electrons would increases gradually to the level of the conventional H-modes, while the density gradient changes insignificantly.

* Authors to whom any correspondence should be addressed.

Meanwhile, edge fluctuations with middle range frequency around 50–100 kHz disappear and turbulence with broad frequency band pops up in the high range around 150–400 kHz in lab frame and is believed to play a major role in sustaining the two decoupled transport channels and the whole I-mode regime. These high frequency fluctuations are termed weekly coherent mode (WCM), which can be detected from the signals of fluctuations of density, temperature as well as poloidal magnetic field. Typically, the relative fluctuation level of density in I-mode is about 10%, that of magnetic field less than 1% and that of temperature around 1% [6–8]. Recently I-mode plasmas with features similar to those on C-Mod have also been created on DIII-D [4], ASDEX Upgrade [3] and EAST [5].

Further follow-up investigations on I-mode plasmas from the theorical, simulation as well as experimental aspects [9–15] have provided some preliminary understandings of this regime. Coppi and Zhou [9, 10] proposed a model in which the WCM was treated as a type of heavy impurity mode, which can 'purify' the plasmas through the outward transport of this heavy species. Reinke *et al* [15] also demonstrated that small amounts of impurities have a dramatic effect on the I-mode fluctuations and operation. Cziegler *et al* [7] identified the co-existing lower frequency mode with geodesic acoustic mode (GAM), which sucks energy from WCM turbulence and widens the frequency band of the latter. Through BOUT++ simulation, Liu *et al* [12] concluded that WCM turbulence is 'resistive ballooning mode (RBM) and drift alfvenic mode dominant'.

We know that a complete and self-consistent physical picture of I-mode is very important to seek for its possible application in the future fusion plasma operation. Challenging issues like the essence of WCM, the mechanisms responsible for L–I transitions, the decoupling of heat and particle transport channels needs to be tackled. Since the steady I-mode has been achieved for the first time on Alcator C-Mod [2], a compact tokamak with high plasma density and high toroidal field, this regime has been produced over essentially all the magnetic fields achievable on this tokamak [16]. The high field approach is much easier in accessing and sustaining the I-mode regime and is drawing more and more attention. Beginning with the pioneering Alcator A machine built in 1970s and followed by its several upgrades, this approach has evolved into the burning plasma grogram called Ignitor, led by Coppi [17, 18], in which running the I-mode regime has been scheduled. Recently Whyte *et al* also launched another programme named SPARC [19]. These programs emphasize particularly the high field and compact approach to burning plasmas, to quickly advance research in this respect.

In view that there is no consensus even on the nature of WCM turbulence, it is worthwhile to launch first principle simulations with the experimental I-mode edge profiles and parameters, which directly motivates our work. The primary goal of this paper is to investigate the fluctuations and their transport properties in the I-mode plasmas through massive gyrokinetic simulations using gyrokinetic toroidal code (GTC) [20]. We have conducted a series of global gyrokinetic simulations, using the profiles from the discharge #1120907032 on Alcator C-Mod [12, 21]. Since in the I-mode plasmas the density fluctuation level is much higher than that of magnetic fluctuation and the local β_e is estimated to be less than 0.1% around the temperature pedestal of the I-mode, the reasonable electrostatic approximation will be adopted as a first attempt of our I-mode study via gyrokinetic simulation. Given the characteristic frequencies and wavelengths of the I-mode plasma fluctuations, the ion response is described by gyrokinetics and that of the electron by drift kinetics [20, 22], and both passing and trapped particles are retained in the simulation.

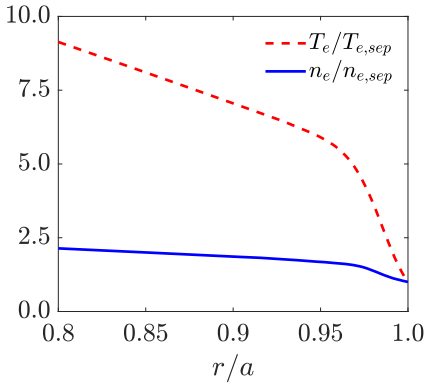

Figure 1. Edge temperature and density profiles of I-mode [12,21].

The simulation domain is restricted in the edge region of tokamak around 0.8–0.99 minor radius of the plasma column with $R_0 = 0.67$ m, $a = 0.22$ m where the WCM and temperature pedestal are located (figure 1). The two normalized gradient length scales of local electron and ion temperatures are taken as $R_0/L_{\mathrm{Te}} = R_0/L_{\mathrm{Ti}} = 142$, and those of local density as $R_0/L_{\mathrm{ne}} = R_0/L_{\mathrm{ni}} = 42$. Other parameters adopted are $T_{\mathrm{e},95} = 700$ eV, $n_{\mathrm{e},95} = 1 \times 10^{20}$ m^{-3}, local safety factor $q_{95} = 3.5$ and on-axis magnetic field $B_0 = 5.8$ T, which gives rise to the local ratio $a/\rho_{\mathrm{s}} = 472$ with gyroradius $\rho_{\mathrm{s}} \equiv C_{\mathrm{s}}/\Omega_{\mathrm{c}}$ at the reference point, where ion sound speed $C_{\mathrm{s}} \equiv \sqrt{T_{\mathrm{e}}/m_{\mathrm{p}}}$, m_{p} is the proton mass and $\Omega_{\mathrm{c}} = eB_0/m_{\mathrm{p}}$. We choose deuteron (D) as the ion species in the simulation and first treat the plasmas to be collisionless. Collisional effects will be investigated in section 5. Albeit impurity ions may be important to I-mode [9, 10, 15], we ignore them in our simulations as a first attempt to study the I-mode physics. By ignoring plasma shaping, the magnetic flux surfaces are simply assumed to be concentrically circular.

2. Validation of I-mode edge properties

To validate nonlinear GTC simulation, we need to compare turbulence characteristics and transport levels from the simulation with the experimentally featured in I-mode plasmas. Here we list a number of important characteristics of the I-mode plasmas from C-Mod discharge #1120907032: there exist characteristic turbulent fluctuations called WCM, which propagate in electron diamagnetic drift (EDD) direction with frequency around 150–400 kHz in the lab frame; it is also observed that a GAM coexists with the WCM; the effective heat diffusivity is calculated to be about 0.15–0.35 m^2 s^{-1},

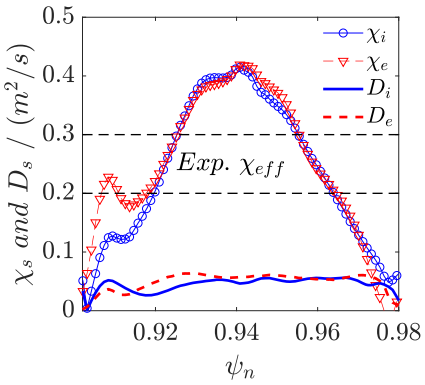

Figure 2. Radial profiles of ion/electron heat diffusivities χ_i/χ_e and particle diffusivities D_i/D_e.

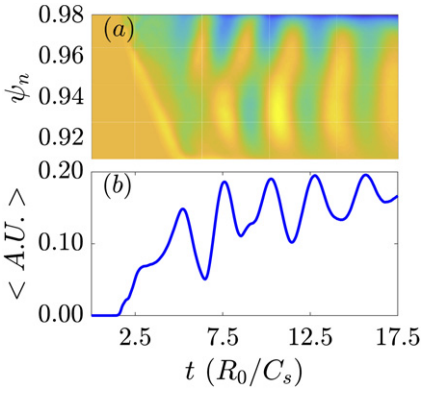

Figure 3. (a) Radial potential structures of GAM/LFZF and their time evolutions; (b) time evolution of GAM/LFZF intensity at the diagnostic point $r = r_{\rm ref}, \theta = 0, \zeta = 0$.

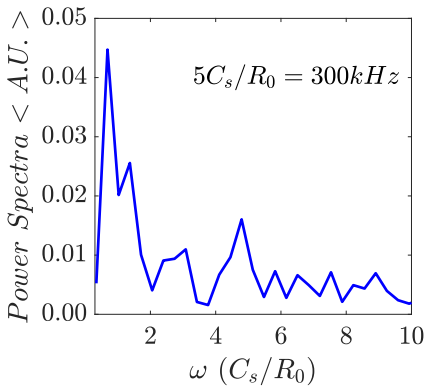

Figure 4. Power spectrum of electrostatic potential at $r = r_{\rm ref}$, $\theta = 0$ and $\zeta = 0$. The peaks around $\omega = 0.5, 1.4, 4.8$ (in unit $C_{\rm s}/R_0$) are identified with LFZF, GAM and WCM-like signal, respectively.

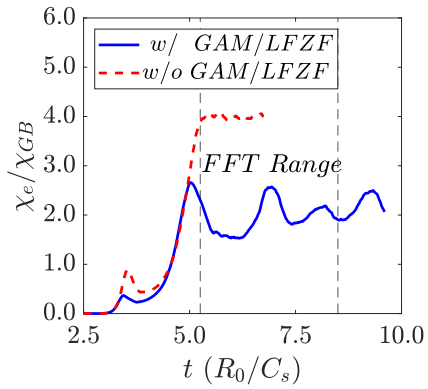

Figure 5. Time evolution of the electron heat diffusivity induced by WCM-like turbulence and the regulation role of GAM/LFZF on it. Bounded by the two vertical dashed lines is the time window in which the power spectra over frequency have been analysed, as shown in figure 4.

while the particle transport is about 0.05 $m^2\ s^{-1}$, which is lower than the particle transport coefficient measured from experiments (about 0.1 $m^2\ s^{-1}$) [23].

As shown in figure 2, our nonlinear simulation successfully demonstrates that the nonlinear edge heat diffusivities for ion and electron, $\chi_{\rm i}$ and $\chi_{\rm e}$, are at the same level as the experimental values. However, the particle diffusivities for both species, $D_{\rm i}$ and $D_{\rm e}$, are significantly lower than those from experiment diagnostics. This suggests that the particle and energy transport decoupling observed in the I-mode experiment cannot be reproduced by gyrokinetic simulation in the electrostatic limit. This may further imply that the dominant turbulence such as the WCM-like turbulence could not be completely treated as electrostatic, although the edge density fluctuation level of WCM-like turbulence is one order of magnitude higher than that of poloidal magnetic field and the edge local $\beta_{\rm e}$ value is small enough, for which the traditional drift wave turbulence can be safely treated as electrostatic. Surprisingly, we found that the turbulence driven by the I-mode profiles can self-generate GAM oscillations and LFZF, that have been observed in all I-mode experiments [24]. Shown in figures 3(a) and (b) are the evolution of the perturbed electrostatic potential averaged over the reference magnetic surface, where the change of colour with time over the narrow edge region in the form of strips indicates that there exists the component of oscillations with mode numbers $n = 0$ and $m = 0$, which is for GAM and LFZF. Simple estimation based on the periodic change shown in figures 3(a) and (b) reveals that the frequency normalized to GAM frequency predicted from ideal magneto-hydrodynamics is $\omega_{\rm GAM}^{\rm simulation} \simeq 1.45\omega_{\rm GAM}$ with $\omega_{\rm GAM}^2 \approx R_0^{-2}(2 + q^{-2})\gamma T/m_{\rm i}$ [25], which is very close to the characteristic order of GAM. Shown in figure 4 is the frequency spectrum during nonlinear saturation process in the temporal window bounded by the two vertical dashed lines in figure 5. This spectrum ranges over a WCM-like signal near the frequency $4.8C_{\rm s}/R_0$, a GAM signal near the frequency $1.6C_{\rm s}/R_0$ and extremely low frequency for LFZF.

3. Turbulence saturation mechanisms and roles of GAM/LFZF

In the performed nonlinear validation simulations, we find out that the turbulence saturates twice in succession, one phase of gently linear growth and saturation followed by another phase of more explosive linear growth and saturation, which is somewhat atypical, as illustrated by the solid-blue line in figure 5

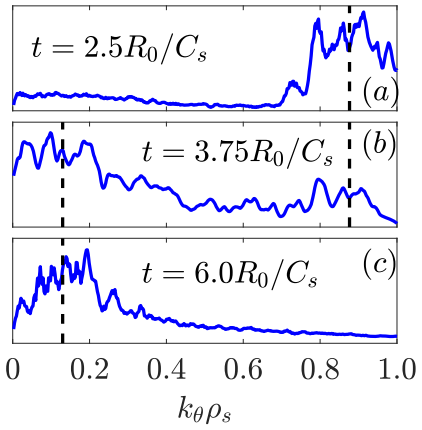

Figure 6. Poloidal spectra measured at three moments corresponding to those for the solid-blue curve in figure 5.

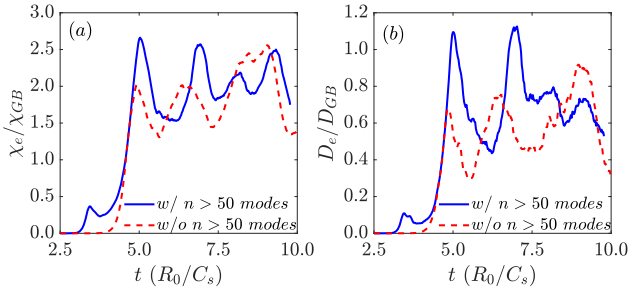

Figure 7. Simulation with shorter wavelength modes filtered out yields almost the same final saturation level as that retaining full poloidal spectra. (*a*) Time history of electron heat diffusivity. (*b*) Time history of electron particle diffusivity.

for the time evolution of the electron heat diffusivity. This suggests that there may exist two distinct instabilities in two consecutive stages, which are labelled respectively as the first and second instabilities. The first instability dominates the earlier nonlinear process and the second one dominates the later phase, which is a common situation when multi-scale instabilities are considered in the simulation [26–28], and typically all those multi-scale instabilities would influence the final turbulence saturation level substantially together [26]. Besides, in the typical nonlinear saturation process, the dominant unstable mode, which is the most unstable one determined by linear dispersion relation, undergoes exponential growth and gets saturated by wave–wave interaction or wave–particle interaction [29, 30], then the turbulent plasma enters the nonlinear saturation stage and stays in steady state. However, in this nonlinear process shown in figures 5 and 6, right after the first instability becomes saturated and its level gets lowered down somewhat by some dissipation for a while, the second instability is then excited and takes over, which is similar to Howard *et al*'s work [26]. Then the energy transport levels for both species are boosted by another explosive growth of this second instability, to much higher values, e.g., about five times that of the first stage, when new nonlinear saturation is reached.

To verify our judgement that the two instabilities are of different types, we need to examine the time evolution of the mode wavelength for each of them in nonlinear process. The poloidal mode spectra are analysed, as is exhibited in figure 6. Around $t = 2.5R_0/C_s$ in figure 6(*a*), the first unstable mode grows exponentially, which corresponds to the first uphill of the solid-blue curve in figure 5, with central perpendicular wavenumber $k_\theta \rho_s \approx 0.8776$ indicated by the vertical dashed lines in figures 6(*a*) and (*b*). This wavelength is comparable to that of trapped electron mode (TEM) [31–34], which is a typical short wavelength instability, whereas this poloidal wavelength is shorter than that inferred from the WCM. Around $t = 3.75R_0/C_s$, as is shown in figure 6(*b*) which corresponds to the first downhill of the solid-blue curve in figure 5, the spectrum peaks at $k_\theta \rho_s \approx 0.13$ as is marked by the left vertical dashed line. Meanwhile, the peaks around $k_\theta \rho_s \approx 0.8776$ are dwindling drastically relative to the surroundings. We note that $k_\theta \rho_s \approx 0.13$ is very close to the measured poloidal wavenumber of WCM reported in [24]. This means the energy carried by the modes with short wavelengths has been inversely cascaded to the long wavelength WCM-like modes. Around $t = 6R_0/C_s$ and afterwards, the second instability undergoes an exponential growth and reaches a much higher saturation level as is shown in figures 5 and 6(*c*), and the value of $k_\theta \rho_s$ is eventually locked around 0.13 for the WCM-like modes. During the growth of second linear instability and nonlinear saturation the first instability with $k_\theta \rho_s \approx 0.8776$ disappears completely in the poloidal spectra.

On the other hand, when we use some numerical technique to filter out those modes with shorter wavelengths around $k_\theta \rho_s \approx 0.8776$ corresponding to toroidal mode number $n \geqslant 50$ in our nonlinear simulation, the results plotted in figure 7 illustrate that, although the first stage of linear growth and saturation disappears, the final saturation levels of both heat diffusivities and particle diffusivities do not change significantly, comparing with those simulations with shorter wavelength modes retained, which is different from Howard *et al*'s results, where all the multi-scale instabilities concerned in the simulation will affect the final turbulence saturation level and the short wavelength modes cannot be excluded [26]. However, in this work, whether or not the first instability is filtered out, the electrostatic fluctuating potential for WCM-like turbulence maintains almost the same level, and this turbulence potential cascades nonlinearly into the longer wavelength mode with $k_\theta \rho_s \approx 0.13$. This indicates that although the first stage exponential growth of the modes with shorter wavelength ($n \geqslant 50$) raises the transport level by a small amount, apparently, they do not play determining role when the system evolves into the ultimate nonlinear saturation phase. Therefore, between the two instabilities with distinct spatial scales, it is the mode with $k_\theta \rho_s \approx 0.13$ that determines the transport level, and hence might be identified with the dominant linear mode for the WCM-like turbulence reproduced in our GTC simulations with the I-mode plasmas profiles on C-Mod.

It is well-known that GAM/LFZF has the capability of regulating turbulence and improving confinement quality indirectly. One naturally expects that the regulation of GAM/LFZF remains valid for the I-mode. In fact, the experiments [7,

24, 35] have revealed that: (1) GAM sucks energy from the WCM turbulence and broadens the frequency band of the latter through nonlinear interaction; (2) GAM and WCM vanish simultaneously when the plasmas transit from I-mode to the flow-up ELM-free H-mode when heating power is above some threshold [3, 6]. However, it remains elusive to what extent the regulating role is played by GAM/LFZF in I-mode plasmas. We therefore conduct two contrasting nonlinear simulations to examine the influences of GAM/LFZF on WCM-like turbulence and its transport properties. In one of such simulations, we calculate the electron heat diffusivity induced by the WCM-like turbulence with the self-generated GAM/LFZF retained and the time history of this transport coefficient is plotted in figure 5 as solid-blue curve, in the other the response of GAM/LFZF is filtered out and the resultant electron heat diffusivity by turbulence alone is shown in figure 5 as dashed-red curve. By comparison of these two cases, we find out that both the first and second instabilities are strongly regulated by GAM/LFZF. However, the second instability is evidently affected more, as not only its saturation level drops down more but also it oscillates more violently, after reaching its peak value when entering the nonlinear phase.

4. Linear physics of I-mode

Following the traditional procedure of exploring generic nonlinear physics, in order to gain deeper understanding of this WCM-like turbulence, it is not sufficient to work on the nonlinear simulation alone. In fact, we conduct a series of linear simulations to see how the linear dispersion relation behaves and to identify the dominant unstable mode at each linear stage of the two distinct evolution processes in our previous nonlinear simulation.

4.1. Linear dispersion relation of the instabilities

In our linear simulations, we first work on single fixed toroidal mode number n to capture the most unstable poloidal mode, and then vary the n number to get the frequency and linear growth rate for each mode that needs to be identified. Firstly, we retain all ingredients of gyrokinetic ion response and all those of drift-kinetic electron in our linear simulations. In this case, as shown in figure 8(b), there are two comparable peaks of linear growth rate located around $k_\theta\rho_s \approx 0.16$ and $k_\theta\rho_s \approx 0.85$, respectively, i.e., the two normalized poloidal wave numbers marked in figure 6 for the two dominant instabilities in the preceding nonlinear simulations. Thus, the linear instability with maximum growth rate around $k_\theta\rho_s \approx 0.85$ corresponds to the first exponentially growing phase shown in figure 5, and the one with peaked growth rate around $k_\theta\rho_s \approx 0.16$ to the second linear growing phase in figure 5, which could accounts for the WCM observed in experiment [23]. Moreover, we note that the linear growth rate for the mode with $k_\theta\rho_s \approx 0.85$ is slightly larger than that with $k_\theta\rho_s \approx 0.16$, and the first unstable mode grows faster and saturates earlier. This is also consistent with our previous observation for the

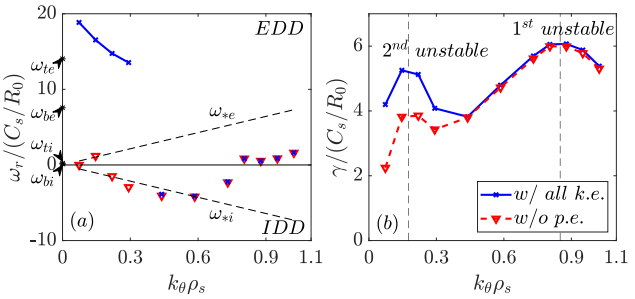

Figure 8. Linear dispersion relations of I-mode edge plasmas. (a) Real frequency ω_r vs $k_\theta\rho_s$. (b) Linear growth rate γ vs $k_\theta\rho_s$. Positive ω_r corresponds to the poloidal mode phase velocity in EDD. Marked on ω_r-axis with asterisks are the heights of ω_{te}, ω_{be} ω_{ti} and ω_{bi}. The blue crosses are for the case in which non-adiabatic response of passing electrons are retained while the red triangles for the case otherwise.

dynamic evolution of these two modes in the nonlinear saturation process, that is, the more unstable mode exponentially grows faster and saturates earlier in its nonlinear evolution.

Upon inspecting the mode frequencies and the directions of phase velocity shown in figure 8(a), we find out that there are three categories of modes: (1) the most unstable modes with $k_\theta\rho_s \approx 0.85$, which is marked as '1st unstable' in figure 8(b) and propagates in EDD with frequency in the range of typical ion scale drift instabilities, which could be identified as collisionless trapped electron mode (CTEM) [31–34], which is driven by toroidal precessional resonance; (2) the unstable mode with $k_\theta\rho_s \approx 0.16$, which is marked as '2nd unstable' in figure 8(b) and also propagates in EDD with frequency close to the electron transit frequency ω_{te}; (3) the unstable modes with poloidal wave numbers somewhere between the aforementioned two types ($0.4 < k_\theta\rho_s < 0.8$), which propagates in the ion diamagnetic drift (IDD) direction and have frequencies close to the frequency ω_{*i} or frequency of typical ion drift waves, which could be identified as the toroidal ion temperature gradient (ITG) mode [36–38]. Furthermore, upon switching off the non-adiabatic response of passing electrons and keeping the trapped electron response only, we find out that only the second type unstable mode (the one with highest frequency) are sensitively affected in such a way that both its frequency and linear growth rate drop down substantially. On the other hand, it is well-known that the passing electron response is approximately adiabatic for typical ion drift waves, and the dispersion relation of this type of modes is not expected to be affected sensitively by switching on or off the non-adiabatic passing electron response. The existence of significant non-adiabatic response for the passing electron indicates that this second instability, consistent with the WCM observed experimentally in mode frequency, wavelength, as well as propagation direction, belongs to the type of instabilities that are different from conventional drift waves. It is on our research list to develop a global analytic linear theory for this 2nd unstable mode in the steep gradient pedestal where several characteristic scales are coupled together.

Based on the preceding facts, we conclude that the high frequency branch with longer wavelength ($k_\theta\rho_s \approx 0.16$) is

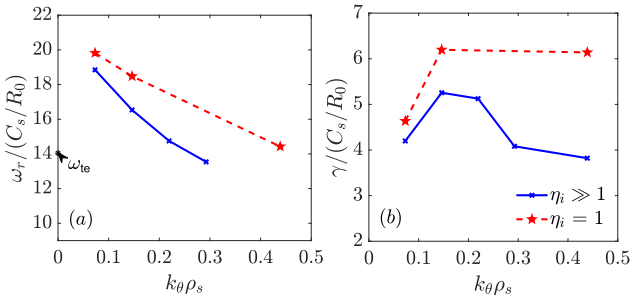

Figure 9. η_i-sensitivity of the higher frequency mode. (*a*) Real frequency ω_r vs $k_\theta\rho_s$. (*b*) Linear growth rate γ vs $k_\theta\rho_s$.The blue cross is for the case with the value of η_i calculated from the I-mode profiles, i.e. $\eta_i \gg 1$, while the red star for the case with $\eta_i = 1$.

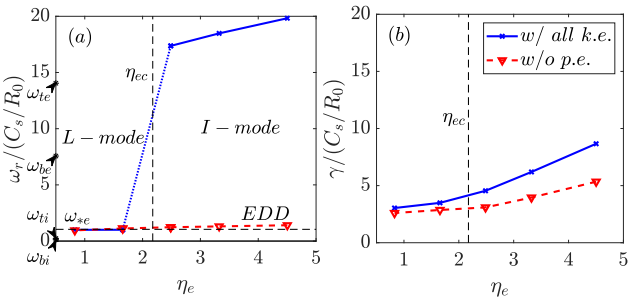

Figure 10. L–I transition and instability-jumping as η_e crosses critical values. (*a*) Real frequency ω_r vs $k_\theta\rho_s$; (*b*) Linear growth rate γ vs $k_\theta\rho_s$.

unlikely to be either TEM or ITG [31–34, 36–38], while the low frequency branch with shorter wavelength ($k_\theta\rho_s \approx 0.85$) should be TEM. In addition, when the relative ITG is lowered down to the value that is comparable to that of ion density ($\eta_i \simeq 1$), shown as the dashed-red curves in figure 9, the high frequency branch persists with slight upswing of frequency. Thus, it is fair to say that the contribution of ITG to this branch is not very relevant. So ITG mode [36–38] must be ruled out as the candidate for WCM at least as long as the linear instability drive is concerned.

4.2. I-mode formation mechanism

Now we focus on the high frequency mode of with $k_\theta\rho_i = 0.16$ or $n = 20$, which is the typical toroidal mode number of WCM observed in the I-mode plasmas on C-Mod [23]. As has been checked in subsection 4.1, the existence of this branch is insensitive to the ITG, thus it can be safely frozen by setting $\eta_i = 1.0$ in the following analysis. We decrease η_e from 4.0 to 1.0 by reducing the electron temperature gradient while keeping electron density gradient fixed. Here the smallest value 1.0 for η_e corresponds to the electron profiles that are almost the same as those of ions, a situation resembling the back transition from I-mode to L-mode. As shown in figure 10(*a*), whether or not the passing electron response is retained in the simulation, there always exists a narrow threshold band of η_e centred around $\eta_{ec} \simeq 2.0$, across which the L–I transition occurs, indicated by the big mode frequency jump. Below this band, the influence of non-adiabatic response of passing electron on the viable instability becomes irrelevant and the corresponding instability should be TEM [31–34] that propagates with characteristic frequency around ω_{*e} in EDD. Meanwhile, the plasma profiles degrade to those for a typical L-mode plasma, which agrees with the common picture that TEM [31–34] grows most easily at the plasma edge for the L-mode plasmas. However, as η_e is increased above the threshold band, the mode frequency jumps up abruptly to the values that are close to the electron transit frequency ω_{te}, which is located in the range of the higher frequency branch aforementioned in section 3 and subsection 4.1. This mode frequency jump seems to agree with the experimental findings [2, 6]: along with the L–I transition and the build-up of edge temperature barrier, there is always an upswing of high frequency band for the WCM turbulence. Moreover, for a wide range of η_e above the threshold band, the non-adiabatic response of passing electrons produces a huge change in the mode frequency as well as a mild change in the growth rate. This heavy dependence on the non-adiabatic component of the passing electrons excludes this mode from some typical drift wave instabilities such as TEM. In this range of η the plasma profiles become similar to those of I-mode plasmas. As we know, the typical I-mode plasmas come with temperature barrier and without particle barrier in the edge region, which complies with a large edge temperature gradient or η_e. Thus, the mode-jumping across critical values of η_e may be relevant to the transition mechanism from L-mode to I-mode or vice versa, and in terms of frequency range, the high frequency mode or its derivative mode is likely to account for the WCM widely observed in the I-mode plasmas. All these similarities cannot simply be counted as just coincidences. Instead, they are solid new evidences that the high frequency mode is most likely to be the dominant linear mode of WCM observed on C-Mod experiments, besides those offered by the nonlinear simulations.

5. Collisional effects

So far collisionality has been completely ignored in our simulation. In the I-mode plasmas, the edge temperature is significantly lower than the core temperature, which is similar to conventional H-mode plasmas. Although the density profile of I-mode plasma is as flat as the L-mode plasmas, in C-Mod the plasma density is higher than other machines like EAST. The edge collisionality is expected to be higher than that in the core region and in other machines. Hence the edge plasmas may not be collisionless and it is better to check how the collisionality affects the instability and transport in the I-mode plasmas. To this end, the collisional effects is implemented by a pitch-angle scattering process for electrons in the simulation, with the local effective electron collision frequency $\nu_e^* \approx 0.33$ [39–41]. The nonlinear simulation is repeated for this collisional case, and the heat diffusivity, particle diffusivity and GAM/LFZF saturation level are shown in figures 11(*a*)–(*c*). These are contrast plots between the case with collisions (dashed-red curve) and the case without collisions or collisionless (solid-blue curve). The downshifts of the two transport coefficients at each moment and the delayed peaks reveal that both the first and second instabilities are partially stabilized by the electron

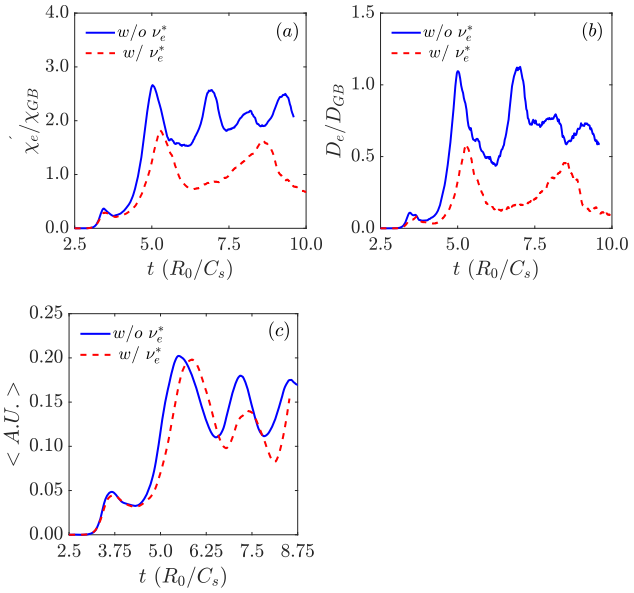

Figure 11. Electron collisional effects on the transport properties in I-mode. (*a*) The electron heat diffusivity is lowered by collisional effects. (*b*) The electron particle diffusivity is lowered by collisional effects. (*c*) The GAM/LFZF saturation level is lowered by collisional effects.

collisional effects. In particular, the nonlinear saturation level of the second instability is lowered down by the collisional effects more enormously and significantly. This difference can also be detected from the GAM/LFZF saturation levels, see figure 11(*c*). For the first exponential growth and saturation, the collisional effect on the GAM/LFZF is marginal. But for the second one, GAM/LFZF are visibly damped by the electron collision, in which the turbulence was supposed to induce more severe transport than the collisionless case [42, 43]. In fact, we observe the contrary trend in the transport level, i.e., the turbulent transport with physical collisions is less than the collisionless turbulent transport shown in figures 11(*a*) and (*b*), which suggests much less linear drive in the case with collisions and the damping effect of collisions play a major role. Therefore, the electron collisional effect in this I-mode scenario is different from that in either dissipative trapped electron mode (DTEM) or RBM, since both DTEM and RBM are normally destabilized by collisional effects in this weak collisional regime. Based on the preceding observations and considerations, both DTEM and RBM can be excluded from the candidates for WCM.

6. Summary and discussion

In this paper we present a novel understanding of the mechanism of I-mode formation and the essence of the associated WCM, based on our electrostatic GTC simulations with the profiles that are taken directly from the experimental I-mode data on C-Mod. In particular, our nonlinear simulations provide two major findings: (1) a long wavelength instability with high frequency in the typical range of local electron transit frequency ω_{te} dominates the nonlinear evolution of the I-mode edge plasmas, and this instability resembles the characteristic WCM in I-mode plasmas in many aspects, such as mode wavelength, frequency spectra of edge fluctuations, the resulting energy transport levels and the associated characteristics of profiles evolution from L-mode to I-mode transitions. The characteristics of this mode and the transport levels out of GTC simulation are listed in table 1 to make comparison with the experimental observations; (2) GAM oscillations with characteristic frequency close to $\omega_{GAM}^2 \approx R_0^{-2}(2+q^{-2})\gamma T/m_i$ are identified to be self-generated by the turbulence nonlinear interaction. Most of this work has been presented in 2019 [44]. Up to now, almost all I-mode experiments have observed that GAM co-exists with WCM fluctuations when plasmas transition from L-mode to I-mode occurs [35]. To our best knowledge, this is the first time that this universal experimental phenomenon has been verified from our first principle gyrokinetic simulations. Meanwhile, the level of effective heat diffusivity out of our simulations is consistent with the experimental values. All these successes strongly suggest that we have captured many essential aspects of the I-mode physics, except that the particle transport level from our simulation is about a half of the experimental value. This implies that the robust transport decoupling of I-mode is hard to be reproduced in the electrostatic simulation in the absence of impurity ions and equilibrium radial electric field.

As for the linear simulation on I-mode, we have discovered a newly unstable mode with high frequency exhibiting many features that are similar to those for WCM. In particular, this mode has a frequency in the range of local electron transit frequency ω_{te} in the plasma frame and propagates in EDD. The mode wavelength is also similar to that of WCM. These two features owned simultaneously by the instability: fast time scale and large space scale together with the non-adiabatically passing electron response exclude TEM, especially CTEM as the candidate for WCM in I-mode plasmas. Furthermore, we find out that finite electron collisional effects can stabilize this mode, so both DTEM and RBM are also ruled out as the candidates. Moreover, since the growth rate of this mode is not sensitive to the local value of η_i, ITG mode [36–38] is also ruled out as the dominant linear instability for WCM. By varying the scale length of electron temperature and density gradient, we have pinpointed this WCM-like mode down to the instability that has long wavelength and high frequency and is driven by electron temperature gradient. All these features strongly suggest that there exist a new type of instability sustaining the I-mode, which is, however, not listed in the zoo of instabilities ever documented before. Further analytical and numerical studies are desired to give a clear identification of this mode.

We note that only conventional two-species plasmas have been considered in this work and impurity ions are excluded in the simulation. However, both theory [9, 10] and experiment [15] suggest that impurity species can play an important role in I-mode plasmas. This is certainly worthy of studying further via simulation, which is on the list of our future work.

Furthermore, due to the closed magnetic flux surfaces adopted around the edge, another important ingredient of I-mode formation, the radial electric field (E_r well), cannot be self-consistently simulated in our present work. According to

Table 1. Characteristics from the C-Mod experiment and GTC electrostatic simulations.

		C-Mod #1120907032	GTC simulation results
WCM	Wavelength	$k_\theta\rho_s = 0.01$–0.3	$k_\theta\rho_s \approx 0.13$
	Frequency	$f = 150$–400 kHz	$f \approx 290$ kHz
	Propagating direction	EDD	EDD
GAM/LFZF		Regulates WCM	Self-generated by turbulence
		Sucks energy from WCM	Regulating turbulence during nonlinear phase
Transport properties	χ_{eff}	0.2–0.3 $m^2\ s^{-1}$	0.15–0.35 $m^2\ s^{-1}$
	D_{eff}	Typically, in the order of magnitude of 0.1 $m^2\ s^{-1}$ [a]	About 0.05 $m^2\ s^{-1}$

[a] This is estimated according to the experimental particle flux Γ in [23].

our understanding, the formation of edge E_r well is mainly induced by direct ion orbit loss at the edge when the plasmas are heated [45–47]. Thus, to self-consistently embrace the effects of E_r well on I-mode plasmas, we may have to run simulations in the realistic unfavourable X-point magnetic geometry, which is also considered as our future work.

Acknowledgments

This work is supported by National MCF Energy R & D Programme of China Nos. 2019YFE03060000 and 2015GB110000, and by NSFC under Grant No. 11975201.

ORCID iDs

Hongwei Yang https://orcid.org/0000-0001-9317-3733

References

[1] Ryter F. *et al* 1998 H-mode power threshold and transition in ASDEX Upgrade *Plasma Phys. Control. Fusion* **40** 725–9
[2] Whyte D.G. *et al* 2010 I-mode: an H-mode energy confinement regime with L-mode particle transport in Alcator C-Mod *Nucl. Fusion* **50** 105005
[3] Ryter F. *et al* 2017 I-mode studies at ASDEX Upgrade: L–I and I–H transitions, pedestal and confinement properties *Nucl. Fusion* **57** 016004
[4] Marinoni A. *et al* 2015 Characterization of density fluctuations during the search for an I-mode regime on the DIII-D tokamak *Nucl. Fusion* **55** 093019
[5] Feng X. *et al* 2019 I-mode investigation on the experimental advanced superconducting tokamak *Nucl. Fusion* **59** 096025
[6] Hubbard A.E. *et al* 2011 Edge energy transport barrier and turbulence in the I-mode regime on Alcator C-Mod *Phys. Plasmas* **18** 056115
[7] Cziegler I. *et al* 2013 Fluctuating zonal flows in the I-mode regime in Alcator C-Mod *Phys. Plasmas* **20** 055904
[8] White A.E. *et al* 2011 Electron temperature fluctuations associated with the weakly coherent mode in the edge of I-mode plasmas *Nucl. Fusion* **51** 113005
[9] Coppi B. and Zhou T. 2011 Heavy particle modes and signature of the I-regime *Phys. Lett.* A **375** 2916–20
[10] Coppi B. and Zhou T. 2012 Interpretation of the I-regime and transport associated with relevant heavy particle modes *Phys. Plasmas* **19** 012302
[11] White A.E. *et al* 2015 Nonlinear gyrokinetic simulations of the I-mode high confinement regime and comparisons with experiment *Phys. Plasmas* **22** 056109
[12] Liu Z.X. *et al* 2016 The physics mechanisms of the weakly coherent mode in the Alcator C-Mod tokamak *Phys. Plasmas* **23** 120703
[13] Mikkelsen D.R., Howard N.T., White A.E. and Creely A.J. 2018 Verification of GENE and GYRO with L-mode and I-mode plasmas in Alcator C-mod *Phys. Plasmas* **25** 042505
[14] liu X. 2018 Gyrokinetic simulation of pedestal turbulence using gene *PhD Dissertation* The University of Texas at Austin
[15] Reinke M.L. *et al* 2019 Radiative heat exhaust in Alcator C-Mod I-mode plasmas *Nucl. Fusion* **59** 046018
[16] Hubbard A.E. *et al* 2017 Physics and performance of the I-mode regime over an expanded operating space on Alcator C-Mod *Nucl. Fusion* **57** 126039
[17] Bombarda F., Coppi B., Airoldi A., Cenacchi G. and Detragiache P. (Ignitor Project Group) 2004 Ignitor: physics and progress towards ignition *Braz. J. Phys.* **34** 1786–91

[18] Coppi B. *et al* 2013 New developments, plasma physics regimes and issues for the Ignitor experiment *Nucl. Fusion* **53** 104013
[19] Whyte D. 2019 Small, modular and economically attractive fusion enabled by high temperature superconductors *Phil. Trans. R. Soc.* A **377** 20180354
[20] Lin Z., Nishimura Y., Xiao Y., Holod I., Zhang W.L. and Chen L. 2007 Global gyrokinetic particle simulations with kinetic electrons *Plasma Phys. Control. Fusion* **49** B163–72
[21] Hubbard A.E. *et al* 2016 Multi-device studies of pedestal physics and confinement in the I-mode regime *Nucl. Fusion* **56** 086003
[22] Lin Z. and Chen L. 2001 A fluid-kinetic hybrid electron model for electromagnetic simulations *Phys. Plasmas* **8** 1447–50
[23] Dominguez A. 2012 Study of density fluctuations and particle transport at the edge of I-mode plasmas *PhD Dissertation* Massachusetts Institute of Technology
[24] Cziegler I. 2011 Turbulence and transport phenomena in edge and scrape-off-layer plasmas *PhD Dissertation* Massachusetts Institute of Technology
[25] Winsor N., Johnson J.L. and Dawson J.M. 1968 Geodesic acoustic waves in hydromagnetic systems *Phys. Fluids* **11** 2448
[26] Howard N.T., Holland C., White A.E., Greenwald M. and Candy J. 2015 Fidelity of reduced and realistic electron mass ratio multi-scale gyrokinetic simulations of tokamak discharges *Plasma Phys. Control. Fusion* **57** 065009
[27] Howard N.T., Holland C., White A.E., Greenwald M. and Candy J. 2014 Synergistic cross-scale coupling of turbulence in a tokamak plasma *Phys. Plasmas* **21** 112510
[28] Howard N.T., White A.E., Greenwald M., Holland C. and Candy J. 2014 Multi-scale gyrokinetic simulation of Alcator C-Mod tokamak discharges *Phys. Plasmas* **21** 032308
[29] Horton W. 1999 Drift waves and transport *Rev. Mod. Phys.* **71** 735–78
[30] Dimits A.M. *et al* 2000 Comparisons and physics basis of tokamak transport models and turbulence simulations *Phys. Plasmas* **7** 969–83
[31] Coppi B., Migliuolo S. and Pu Y.K. 1990 Candidate mode for electron thermal energy transport in multi-keV plasmas *Phys. Fluids*B **2** 2322–33
[32] Adam J.C., Tang W.M. and Rutherford P.H. 1976 Destabilization of the trapped-electron mode by magnetic curvature drift resonances *Phys. Fluids* **19** 561–6
[33] Coppi B. and Rewoldt G. 1975 Trapped electron instabilities driven by magnetic curvature drifts *Phys. Lett.* A **54** 301–3
[34] Tang W.M. 1978 Microinstability theory in tokamaks *Nucl. Fusion* **18** 1089
[35] Cziegler I., Hubbard A.E., Hughes J.W., Terry J.L. and Tynan G.R. 2017 Turbulence nonlinearities shed light on geometric asymmetry in tokamak confinement transitions *Phys. Rev. Lett.* **118** 105003
[36] Romanelli F. 1989 Ion temperature-gradient-driven modes and anomalous ion transport in tokamaks *Phys. Fluids* B **1** 1018–25
[37] Coppi B. and Pegoraro F. 1977 Theory of the ubiquitous mode *Nucl. Fusion* **17** 969–93
[38] Tang W.M. and Rewoldt G. 1993 Long-wavelength microinstabilities in toroidal plasmas* *Phys. Fluids* B **5** 2451–9
[39] Hinton F.L. and Hazeltine R.D. 1976 Theory of plasma transport in toroidal confinement systems *Rev. Mod. Phys.* **48** 239–308
[40] Huba J.D. 2009 *NRL Plasma Formulary* (Washington, DC: Office of Naval Research and Naval Research Laboratory)
[41] Sauter O., Angioni C. and Lin-Liu Y.R. 1999 Neoclassical conductivity and bootstrap current formulas for general axisymmetric equilibria and arbitrary collisionality regime *Phys. Plasmas* **6** 2834–9
[42] Hinton F.L. and Rosenbluth M.N. 1999 Dynamics of axisymmetric and poloidal flows in tokamaks *Plasma Phys. Control. Fusion* **41** A653–62
[43] Xiao Y., Catto P.J. and Molvig K. 2007 Collisional damping for ion temperature gradient mode driven zonal flow *Phys. Plasmas* **14** 032302
[44] Yang H., Zhou T., Xiao Y. and Lin Z. 2019 Gyrokinetic simulation of turbulent transport for I-mode edge plasmas CO7 00003 *Bul. APS 61st Annual Meeting APS Division of Plasma Physics* vol 64 (Fort Lauderdale, FL, USA, 21-25 October) (http://meetings.aps.org/link/BAPS.2019.DPP.CO7.3)
[45] Wu G.J. and Zhang X.D. 2012 Calculations of the ion orbit loss region at the plasma edge of EAST *Plasma Sci. Technol.* **14** 789
[46] Wu G.J. *et al* 2014 Fast generation of an inward electric field due to ion orbit losses in the tokamak edge plasma during transition from low-to-high confinement *Nucl. Fusion* **54** 083030
[47] Ku S., Baek H. and Chang C.S. 2004 Property of an X-point generated velocity-space hole in a diverted tokamak plasma edge *Phys. Plasmas* **11** 5626–33